PROCEEDINGS A

royalsocietypublishing.org/journal/rspa

Research

Cite this article: Nguyen HQ, Wu Q, Chen H, Chen JJ, Yu YK, Tracy S, Huang GL. 2021 A Fano-based acoustic metamaterial for ultra-broadband sound barriers. *Proc. R. Soc. A* **477**: 20210024.
https://doi.org/10.1098/rspa.2021.0024

Received: 10 January 2021
Accepted: 31 March 2021

Subject Areas:
mechanical engineering, mechanics, acoustics

Keywords:
Fano resonance, acoustic barrier, transmission loss, coiling-space structure, coupling resonance, effective properties

Author for correspondence:
G. L. Huang
e-mail: huangg@missouri.edu

†These authors contributed equally to the study.

Electronic supplementary material is available online at https://doi.org/10.6084/m9.figshare.c.5393760.

THE ROYAL SOCIETY PUBLISHING

A Fano-based acoustic metamaterial for ultra-broadband sound barriers

H. Q. Nguyen[1,†], Q. Wu[1,†], H. Chen[1], J. J. Chen[1], Y. K. Yu[1], S. Tracy[2] and G. L. Huang[1]

[1]Department of Mechanical and Aerospace Engineering, University of Missouri, Columbia, MO 65211, USA
[2]Materials Innovation, Steelcase Inc., Grand Rapids, MI 49508, USA

HQN, 0000-0002-5368-5993; YKY, 0000-0001-7189-6113; GLH, 0000-0002-6238-6127

Ultra-broadband sound reduction schemes covering living and working noise spectra are of high scientific and industrial significance. Here, we report, both theoretically and experimentally, on an ultra-broadband acoustic barrier assembled from space-coiling metamaterials (SCMs) supporting two Fano resonances. Moreover, acoustic hyper-damping is introduced by integrating additional thin viscous foam layers in the SCMs for optimizing the sound reduction performance. A simplified model is developed to study sound transmission behaviour of the SCMs under a normal incidence, which sets forth the basis to understand the working mechanism. An acoustic barrier with 220 mm thickness is then manufactured and tested to exhibit ultra-broadband transmission loss overall above 10 dB across the range 0.44–3.85 kHz, covering completely nine third-octave bands. In addition, unconventional broadband absorption in the dampened barrier (65%) is experimentally observed as well. We believe this work paves the way for realizing effective broadband sound insulation, absorption and sound wave controlling devices with efficient ventilation.

1. Introduction

Ultra-broadband sound reduction schemes which cover noise spectra in living and working environments are in high demand in both academic and industrial communities [1–6]. Traditional acoustic barriers, which are categorized as either acoustic composite panels [7–9]

or sonic crystals [10,11], have been widely employed. Their performance is fundamentally restricted especially in the low-frequency range, and heavy and bulky designs are usually required. While the former is opaque, the latter interestingly is partially optically transparent and provides ventilation. Principally, there always exists a trade-off between the open ratio, defined as the ratio of the gap between two columns to the lattice constant, and the thickness and performance of a crystal-based sonic barrier [3,12,13]. Previous studies have shown that in order to achieve satisfactory performance, say insertion loss commonly over at least 10 dB [3,14] within the range 0.3–4.0 kHz, an acoustic barrier thickness of at least 0.6 m is required with an open ratio of less than 27% [2,3,12]. These designs are essentially too cumbersome to be employed in real applications, especially in an office or working environment. The main reason for this lies in the fact that they all rely on traditional materials, such as solid, perforated or porous rods deployed on periodic structures. Therefore, new designs with novel materials or structures are necessary in order to overcome the limitations of traditional designs.

In the past two decades, acoustic metamaterials, which refer to artificial resonance-based materials, have been thought of as the most promising candidate to break the traditional materials' limitations in airborne acoustics. In particular, space-coiling metamaterial (SCM) emerges as a special class of metamaterials [15]. It is constructed by coiling up the space within its unit cell to form curled acoustic channels with a subwavelength cross-section. The propagating phase and amplitude can be tuned arbitrarily by adjusting the geometry of the curled channel to give rise to extreme acoustic behaviours, such as an extreme refractive index [16], double-negative media [15] and phase/amplitude modulation [17]. In addition, the SCM was reported to exhibit Fano-like profiles [15]. In general, Fano resonance, first observed by Fano [18], is a special class of coupling resonance which, in most cases, refers to the interference of a local resonance and a background continuum. It comes with a narrow-linewidth asymmetric absorption profile, induced by the intensity interaction and phase-shift involved in inelastic scatterings of electrons in a quantum mechanical setting. In solid mechanics, Fano resonance has been discussed both theoretically and experimentally in several studies [19–21]. In acoustics, however, Fano resonances have been demonstrated visually through asymmetric transmission loss (TL) profiles in simulation and experiments [15,22,23]. A complete theoretical analysis of the formation of Fano resonances specifically by the interference of monopolar/dipolar modes and the background continuum is yet to be established. Two key factors involved in the formation of acoustic Fano resonance are local resonance and coupling of resonances. The former, on the one hand, is generally established by satisfying input impedance matching conditions (zero reactance) [8,13,24] and exhibits extreme and unnatural effective constitutive properties [25–28]. The latter, on the other hand, is a consequence of interaction of multiple resonances under certain matching conditions. For instance, coupling between two modes of an acoustic resonator results in an anti-resonance with high TL [9,25,29] or a hybrid resonance with perfect absorption [30]. Coupling between resonances from multiple separate resonators also admits perfect absorption [31,32] and allows the existence of multiple double-negative bands [33]. Using Fano resonance, high TL performance was only achieved within a narrow band [23,34,35]. Further exploiting multiple Fano resonances induced by four different Mie resonators [15], a broader band up to 1.25 kHz was observed in numerical simulations. However, the corresponding design with a low open ratio (20%) is still quite thick (0.46 m). To obtain efficient and ultra-broadband TL performance in a compact design, not only fundamental but also higher-order Fano resonances must come into play. That is to say, all of them should be involved and distributed more optimally to cover the broader frequency range of interest [36].

In this research, based on multiple Fano resonances, we propose an acoustic barrier consisting of multiple SCMs to realize ultra-broadband sound reduction. We first aim to deliver a comprehensive theoretical model to characterize the SCM and the Fano resonance associated with it. The analysis involves replacing the actual SCM with an effective model which contains an effective, straightened channel filled with slow-wave materials. The effective channel, which supports both monopolar and dipolar modes, interacts with the background continuum, giving rise to Fano resonances. Because of their coupling nature, the effective model is hence called

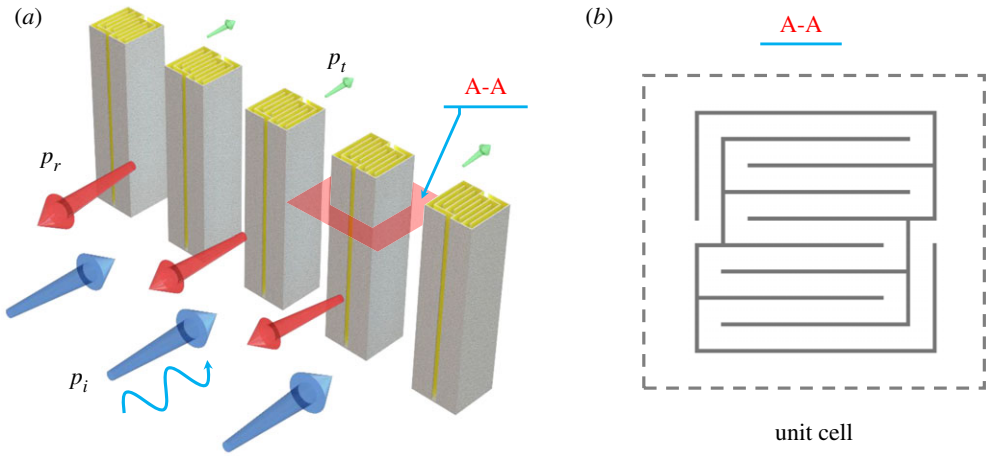

Figure 1. (*a*) Schematic illustration of the acoustic barrier assembled from SCMs. It efficiently blocks the incoming sound waves (p_i) indicated by the blue arrows. The substantially reflected (p_r) and heavily suppressed transmitted (p_t) sound fields are indicated by red and green arrows, respectively. (*b*) Sectional view of the cross-section of an SCM unit cell. (Online version in colour.)

a coupling unit throughout the paper. The Fano resonances are thoroughly studied using a transfer matrix method and effective medium theory, and are fully characterized in terms of TL. Corresponding numerical simulations are then conducted to validate the theoretical prediction and also to better illustrate the Fano-resonance-based broadband sound reduction. Lastly, we construct an acoustic barrier using the proposed SCMs with different geometrical properties, and conduct experiments to demonstrate potential applications of ultra-broadband sound reduction.

2. Theoretical formulation of Fano-based metamaterials

The Fano-based acoustic barrier consists of arrays of the SCMs, as shown in figure 1*a*. It is designed such that the incoming sound waves are efficiently blocked over a broad frequency range, achieving broadband high TL. The broadband nature of the acoustic barrier originates from multiple Fano resonances supported by the SCM coupling unit. As illustrated in figure 1*b*, the design of the SCM unit cell involves two identical ventilation channels located on the top and bottom of the coupling unit and a curled channel connecting the upstream and downstream with a space-coiling path. Space-coiling designs are usually used to generate linear resonances with optimal occupied space [8] and present an excellent capability to control the frequency distribution of not only fundamental but also higher-order modes [36,37]. In this work, these strategies are employed to manipulate the local resonances and the resulting Fano resonances uniformly over the frequency region of interest.

To study acoustic wave transmission and reflection behaviour of the acoustic barrier, we introduce a simplified acoustic model of the SCM unit with the rigid side-wall boundary conditions shown in figure 2 subjected to a normal incidence $p_i = P_i\,\mathrm{e}^{-\mathrm{i}kx}$. In the simplified model, the actual curled channel is replaced with a straightened effective channel filled with effective fluid. The effective fluid is characterized by constitutive parameters (ρ_e and c_e) such that the weight of fluid inside the channel and sound travelling time in the two channels are guaranteed identical [15]. The ventilation channels are filled with air (ρ_0 and c_0).

The effective channel behaves as a linear resonator supporting both monopolar and dipolar local resonances [8,34]; however, the ventilation channels only support resonances at higher frequencies and the acoustic pressure is linear in terms of phase change at lower frequencies. The transmission is the radiation from channels to the downstream, while the reflection is the

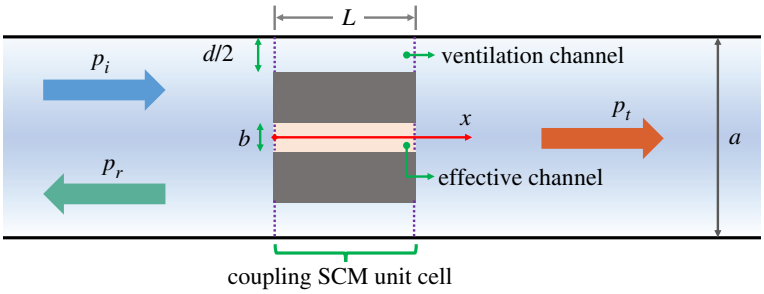

Figure 2. Schematic of an effective SCM coupling unit cell submerged in an impedance tube. p_i, p_r and p_t represent the incident, reflected and transmitted pressure fields, respectively. (Online version in colour.)

combination of the radiation from the channels to the upstream and the reflection by the external hard wall of the coupling unit [29,38] as

$$p_t(x,y) = p_d \quad \text{and} \quad p_r(x,y) = P_i\,\mathrm{e}^{\mathrm{i}kx} + p_u, \tag{2.1}$$

where p_u and p_d are the radiation fields in the upstream and downstream, respectively. They are related to the velocities at the inlet ($x = 0$) and outlet ($x = L$) of the channels via Green's functions [13],

$$p_u\left(x,y\right) = -\mathrm{i}\rho_0 c_0 k v_{e1} \int_{-b/2}^{b/2} G_u\left(x,y|0,y_0\right)\,\mathrm{d}y_0 - 2\mathrm{i}\rho_0 c_0 k v_{v1} \int_{a/2-d/2}^{a/2} G_u\left(x,y|0,y_0\right)\,\mathrm{d}y_0 \tag{2.2a}$$

and

$$p_d\left(x,y\right) = \mathrm{i}\rho_0 c_0 k v_{e2} \int_{-b/2}^{b/2} G_d\left(x,y|L,y_0\right)\,\mathrm{d}y_0 + 2\mathrm{i}\rho_0 c_0 k v_{v2} \int_{a/2-d/2}^{a/2} G_d\left(x,y|L,y_0\right)\,\mathrm{d}y_0. \tag{2.2b}$$

Here, (v_{e1}, v_{e2}) and (v_{v1}, v_{v2}) are the velocities of the effective and ventilation channels at their inlet and outlet, respectively. $G_u(x,y|0,y_0)$ and $G_d(x,y|L,y_0)$ are the Green's functions of the upstream ($x < 0$) and downstream ($x > L$). They can be presented in terms of the mode shape functions of the waveguide [38,39],

$$G_u\left(x,y|0,y_0\right) = \frac{1}{\mathrm{i}ka}\left\{\mathrm{e}^{\mathrm{i}kx} + \mathrm{i}\sum_{n=1}^{\infty} \frac{\varphi_n\left(y\right)\varphi_n\left(y_0\right)}{\alpha_n\left\langle\varphi_n^2\left(y\right)\right\rangle}\,\mathrm{e}^{\alpha_n x}\right\} \tag{2.3a}$$

and

$$G_d\left(x,y|L,y_0\right) = \frac{1}{\mathrm{i}ka}\left\{\mathrm{e}^{-\mathrm{i}k(x-L)} + \mathrm{i}\sum_{n=1}^{\infty} \frac{\varphi_n\left(y\right)\varphi_n\left(y_0\right)}{\alpha_n\left\langle\varphi_n^2\left(y\right)\right\rangle}\,\mathrm{e}^{-\alpha_n(x-L)}\right\}, \tag{2.3b}$$

where φ_n and α_n are the nth-order mode shape function and corresponding eigenfrequency of the waveguide's cross-section, respectively (see electronic supplementary material). Assuming that the effective and ventilation channels are narrow, the pressure fields inside them can be estimated by the fundamental mode [13] as

$$p_e\left(x\right) = A_e\,\mathrm{e}^{-\mathrm{i}k_e x} + B_e\,\mathrm{e}^{\mathrm{i}k_e(x-L)} \tag{2.4a}$$

and

$$p_v\left(x\right) = A_v\,\mathrm{e}^{-\mathrm{i}kx} + B_v\,\mathrm{e}^{\mathrm{i}k(x-L)}, \tag{2.4b}$$

respectively, where A and B are the amplitude coefficients by linearity in the channels and the wavevector of the effective channel $k_e = \omega/c_e$. The relations between the velocities and the pressures of the channels at their inlet and outlet are obtained by applying Euler's equation $\rho(\partial\vec{v}/\partial t) = -\nabla p$. Substituting equation (2.4) into equations (2.1) and (2.2) leads to the following set

of equations in a matrix form for determining the normalized volume velocities at the inlet/outlet of the channels:

$$\boldsymbol{M}\begin{bmatrix}\bar{v}_{e1}\\ \bar{v}_{e2}\\ \bar{v}_{v1}\\ \bar{v}_{v2}\end{bmatrix}=\begin{bmatrix}2\\0\\2\\0\end{bmatrix}, \tag{2.5}$$

where the normalized volume velocities $\bar{v}_{e1}$, $\bar{v}_{e2}$, $\bar{v}_{v1}$ and $\bar{v}_{v2}$ are defined by $\bar{v}=\sigma\rho_0 c_0 v/P_i$ with σ being the open ratio of the corresponding channels. $\boldsymbol{M}$ is a 4×4 matrix representing the coupling between the radiation fields of the channels (see electronic supplementary material). Considering $|x|\to\infty$, equations (2.1) and (2.2) result in the expressions of transmission and reflection in the far field,

$$p_t(x)=P_i(\bar{v}_{e2}+\bar{v}_{v2})\,\mathrm{e}^{-\mathrm{i}k(x-L)} \tag{2.6a}$$

and

$$p_r(x)=P_i(1-\bar{v}_{e1}-\bar{v}_{v1})\,\mathrm{e}^{\mathrm{i}kx}, \tag{2.6b}$$

respectively. As a result, the transmission and reflection coefficients are readily obtained as

$$T=\bar{v}_{e2}+\bar{v}_{v2}\quad\text{and}\quad R=1-\bar{v}_{e1}-\bar{v}_{v1}, \tag{2.7}$$

respectively. Now, we consider an effective homogeneous medium representing the coupling unit under the long-wavelength assumption. The effective medium is acoustically characterized by the effective mass density ρ_{eff} and the effective bulk modulus B_{eff}, which can be retrieved using the scattering matrix approach [40],

$$\begin{bmatrix}P_1\\U_1\end{bmatrix}=\begin{bmatrix}\cos(k_{\mathrm{eff}}a) & \mathrm{i}Z_{\mathrm{eff}}\sin(k_{\mathrm{eff}}a)\\ \mathrm{i}Z_{\mathrm{eff}}^{-1}\sin(k_{\mathrm{eff}}a) & \cos(k_{\mathrm{eff}}a)\end{bmatrix}\begin{bmatrix}P_2\\U_2\end{bmatrix}, \tag{2.8}$$

where P_1, U_1 and P_2, U_2 are the total pressure and velocity fields evaluated on the left and right sides of the effective medium. Solutions to equation (2.8) lead to the effective velocity, impedance, mass density and bulk modulus, respectively, being

$$c_{\mathrm{eff}}=\frac{\omega}{k_{\mathrm{eff}}}=\frac{\omega a}{\cos^{-1}[(P_1U_1+P_2U_2)/(P_1U_2+P_2U_1)]}, \tag{2.9a}$$

$$Z_{\mathrm{eff}}=\mathrm{i}\frac{P_2^2-P_1^2}{P_1U_2+P_2U_1}\sqrt{\frac{(P_1U_2+P_2U_1)^2}{(P_2^2-P_1^2)(U_1^2-U_2^2)}} \tag{2.9b}$$

and

$$\rho_{\mathrm{eff}}=\frac{Z_{\mathrm{eff}}}{c_{\mathrm{eff}}}\quad\text{and}\quad B_{\mathrm{eff}}=Z_{\mathrm{eff}}c_{\mathrm{eff}}. \tag{2.9c}$$

To validate the above analysis, an effective unit cell with $a=88.89$ mm, $b=11$ mm, $d=26$ mm, $L=63$ mm and $\rho_e/\rho_0=c_0/c_e=4.375$ is investigated theoretically and numerically. The numerical simulation is conducted using COMSOL Multiphysics. To investigate the Fano resonance involved and its associated sound reduction application, TL, defined as $20\times\log_{10}|p_i/p_t|$, is assigned as the characterization measure of the sound reduction performance. Excellent agreement between the analytical and numerical TL spectra can be observed in figure 3*a*, proving the correctness of our theoretical model. As illustrated in figure 3*a*, two asymmetrical profiles of TL peaks and dips of the unit are clearly observed, similar to the Fano-like resonance. Note that the high TL region can be formulated between the two TL peaks for broadband sound mitigation if we design the unit cell properly. Those two asymmetric transmission profiles are due to the fact that the portion of the acoustic wave travelling through the resonating effective channel interferes with the portion of the acoustic wave travelling through the non-resonating ventilation channel. The asymmetric transmission profile, based on a Fano-like interference, possesses a peak region due to destructive interference resulting in attenuation of the transmitted wave.

The TL peaks and dips, from another point of view, can be considered as the resonances and anti-resonances of the unit cell, respectively [13,38]. The working mechanism of the unit cell at

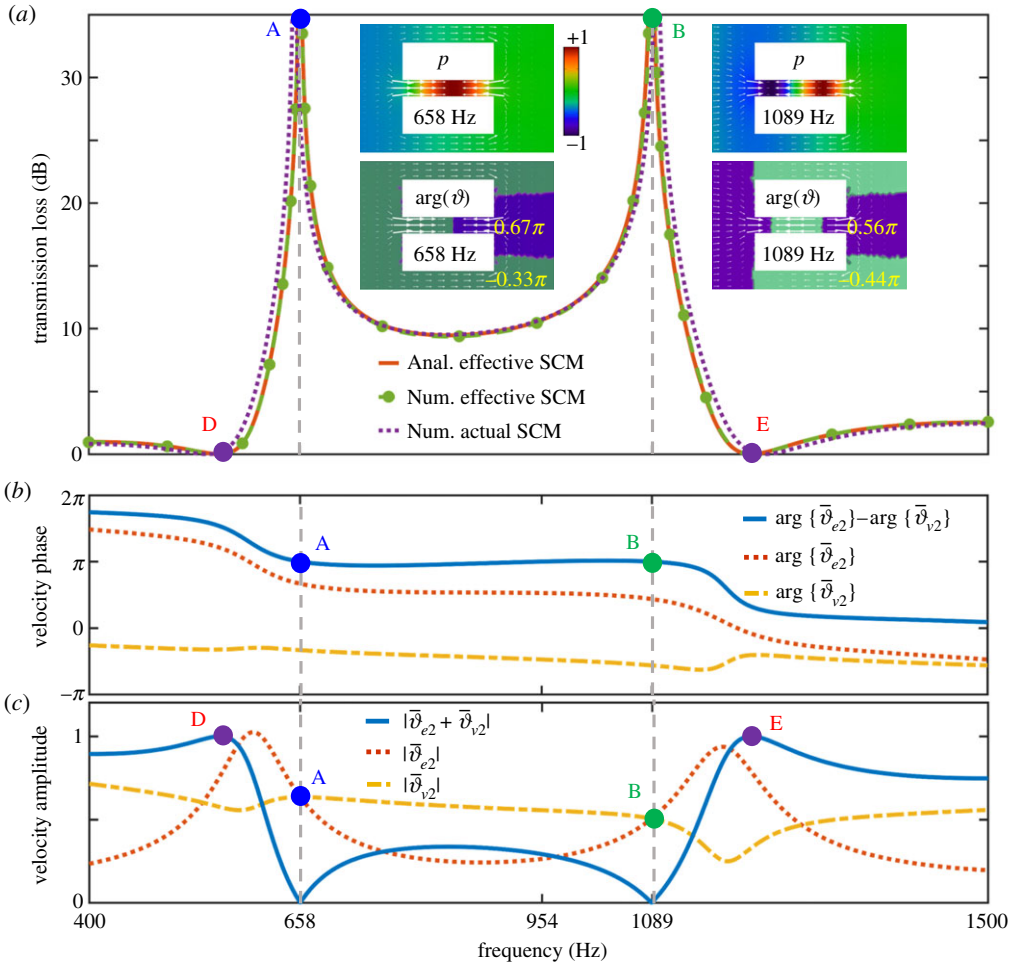

Figure 3. (*a*) TL spectra of the effective SCM unit cell. Theoretical and numerical results are shown, together with the numerical result of the actual SCM unit cell. At the two TL peaks, both the magnitude and phase of the velocity distributions of the effective SCM coupling unit are illustrated as insets. (*b*) Frequency-dependent phase spectra of the normalized volume velocities $\bar{v}$ at the outlet of the channels. (*c*) Frequency-dependent amplitude spectra of the normalized volume velocities $\bar{v}$ at the outlet of the channels.

low frequencies can be explained by the weakly coupled effective and ventilation channels. For the interested frequency regime, the effective channel supports two local modes, i.e. monopolar and dipolar, evidenced by two TL dips at 560 Hz and 1121 Hz, respectively, while the ventilation ones support an acoustic linear flow in terms of the phase change, evidenced by the smooth TL profile (see electronic supplementary material). The coupling between these two channels induces resonance and anti-resonance in the unit cell. Since the former is much stronger than the latter, the induced resonance and anti-resonance are located in the close vicinity of the local resonances of the effective channel. Therefore, the mode shape of the TL peaks and dips are mainly characterized by the mode shapes of the effective channel local resonances (see the pressure field (*p*) described in the inset of figure 3*a*). It is noteworthy that the distributions of the resonances and anti-resonances for the monopolar and dipolar modes are in the opposite order. Specifically, the monopolar mode at 600 Hz and dipolar one at 1121 Hz excite the resonances and anti-resonances of the coupling unit at 560 Hz and 658 Hz and at 1175 Hz and 1089 Hz, respectively, to realize a broadband TL spectrum.

To quantitatively interpret TL peaks and dips, we further plot the phase and magnitude of $\bar{v}$ at the two channel outlets in figure 3*b*,*c*, respectively. According to equation (2.7), the occurrence of TL dips represents the condition $\bar{v}_{e1} + \bar{v}_{v1} = 1$ or $|\bar{v}_{e2} + \bar{v}_{v2}| = 1$, meaning zero reflection. In other words, the total volume velocity transmitted through the inlets is equal to the incident volume velocity (see points D and E on figure 3*c*), which obviously refers to the acoustic impedance matching condition. By contrast, the TL reaches a maximum when the transmission coefficient vanishes. The condition for TL peaks reads $\bar{v}_{e2} + \bar{v}_{v2} = 0$, which indicates that the normalized volume velocities at the outlets of ventilation and the effective channels are identical in amplitude, but are out of phase (see the phase distribution ($\arg(v)$) shown on the inset in figure 3*a* and points A and B on figure 3*b*,*c*). In addition, the normalized acoustic admittance at the outlet of the effective coupling unit, $1/Z_2 = 1/Z_{v2} + 1/Z_{e2} = \bar{v}_{v2}/p + \bar{v}_{e2}/p$, is zero, indicating that the normalized acoustic impedance, $Z_2 \to \infty$, and the outlet now are equivalently an acoustically rigid wall. In this case, the effective coupling unit blocks all the incoming pressure fields, leading to transmission zeros. Finally, as illustrated in figure 3*b*,*c*, the phase difference between $\bar{v}_{e2}$ and $\bar{v}_{v2}$ is nearly constant (π) in the region between points A and B while their amplitudes show small difference. Therefore, high TL in the region between two peaks can be expected.

The excellent sound reduction performance can also be explained using an effective medium. Following equation (2.9), we plot the real part of the normalized effective density $\rho^*_{\text{eff}} = \text{Re}\{\rho_{\text{eff}}/\rho_0\}$ and bulk modulus $B^*_{\text{eff}} = \text{Re}\{B_{\text{eff}}/B_0\}$ in figure 4*a*. Two separate single-negative stop bands (SNBs), i.e. a negative density region (590–733 Hz) and a negative bulk modulus region (936–1178 Hz), can be seen. The negative bulk modulus is responsible for the first Fano resonances with the monopolar mode and the negative density can be used to capture the second Fano resonances with the dipolar mode. The normalized decaying factor (NDF), defined as $\gamma^*_{\text{eff}} = \text{Im}\{-k_{\text{eff}}a\}$, is presented in figure 4*b*. It can be observed that γ^*_{eff} is zero everywhere except within the SNBs, whereas $\text{Re}\{k_{\text{eff}}\}$ (not shown here), which represents the propagating part of the sound wave, is zero within SNBs and positive at other frequencies. Within the SNB regions, the NDF takes large values and reaches a maximum at the Fano resonances, meaning that the wave amplitude exponentially decays. In brief, the two Fano resonances result in two SNBs providing considerably high TL, efficiently blocking the sound field.

3. Dampened space coiling metamaterial

Although the combination of two symmetrical Fano-like profiles leads to a broadband TL spectrum, two dips corresponding to two coupling resonances of the coupling unit still need to be fixed to optimize the performance of an acoustic barrier built from an array of coupling units. For real applications, which often require an ultra-broadband working region, the previously achieved TL profile is not optimal. Weakening the local resonances gives weaker Fano resonances, lifting the TL dips but inevitably lowering the peaks simultaneously. This process results in a more practically optimal TL profile. Dampening the SCM is the most straightforward way to weaken the local resonances. In theory, this can be achieved by considering the intrinsic thermal and external acoustic viscosity.

(a) Thermal viscosity

In real structures, there always exists thermal viscosity inside the viscous boundary layers. Its effect is non-negligible around the resonances [6,13] when the induced velocity is large, especially within the SCM where the friction area is massive. The intrinsic thermal viscosity may help to lift the dips of the Fano TL profile, ensuring optimized TL performance within the range of interest. To take into account the thermal viscosity, the density and sound velocity inside the SCM should be modified as [41]

$$\rho_v = \frac{\rho}{\Psi_v} \quad \text{and} \quad c_v = c\sqrt{\frac{\Psi_v}{\gamma - (\gamma - 1)\,\Psi_h}}, \tag{3.1}$$

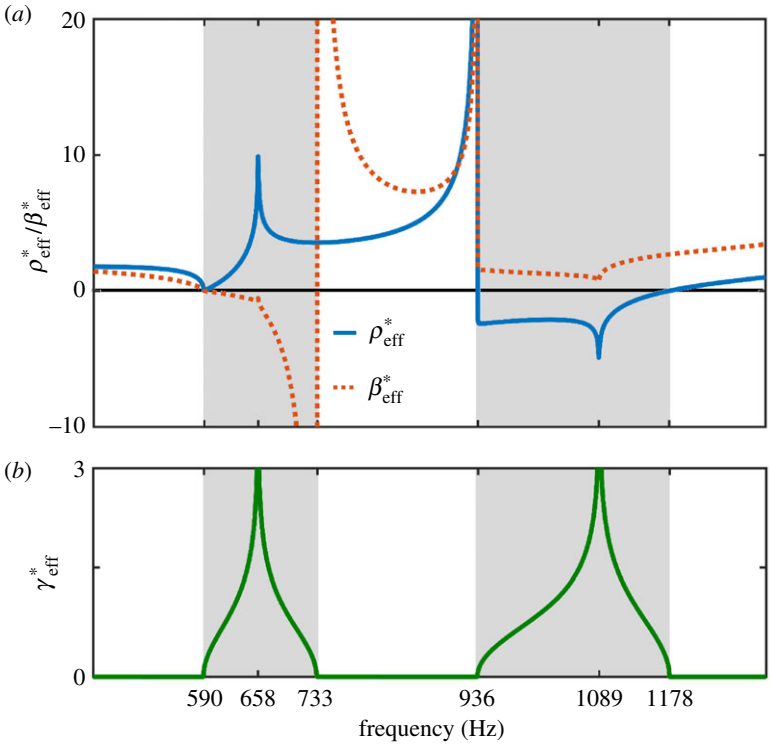

Figure 4. (*a*) Real part of the normalized effective mass density $\rho^*_{\text{eff}} = \text{Re}\{\rho_{\text{eff}}/\rho_0\}$ and the bulk modulus $B^*_{\text{eff}} = \text{Re}\{B_{\text{eff}}/B_0\}$. (*b*) The decaying factor of the unit cell $\gamma_{\text{eff}} = -\text{Im}\{k_{\text{eff}}a\}$. Two single-negative bands are highlighted in grey. (Online version in colour.)

respectively, where Ψ_v and Ψ_h are the viscosity-geometry and thermal-geometry functions for slits,

$$\Psi_v = 1 - \frac{\tan(k_v b/2)}{k_v b/2} \quad \text{and} \quad \Psi_h = 1 - \frac{\tan(k_h b/2)}{k_h b/2}. \tag{3.2}$$

Here, the viscous and thermal lengths are $k_v = \sqrt{-\text{i}\omega\rho/\eta}$ and $k_h = \sqrt{-\text{i}\omega\rho C_p/k}$, respectively, with η being the dynamic viscosity and C_p the heat capacity at constant pressure of air. The thermal viscous effect can be observed in the TL spectra of two cases: the SCMs without (lossless, blue in figure 5*d*) and with viscosity (viscous, red curve in figure 5*d*) applied in the curled channel. They are identical within most regions except around the resonances, as predicted. At the Fano resonances, instead of reaching ∞ in theory, thermal viscosity dampens the resonances, making the peaks less sharp with the maximum TL decreased to less than 35 dB. By contrast, the TL dips are lifted slightly. The thermal viscous effect of these regions can be enhanced using narrower channels with a smaller open ratio b/a. However, narrower channels are usually adverse to improving the TL performance [36]. For practical noise reduction applications, the TL dips should be lifted by using a stronger dampening mechanism.

(b) Acoustic hyper-damping

In this work, acoustic hyper-damping is introduced by deploying acoustic foam layers at the velocity anti-nodes of the SCM, as shown in figure 5*a*. Figure 5*b* exhibits the velocity and pressure profiles, which are opposite to each other in space. The acoustic foam is an open-cell porous material, comprising two phases, i.e. an elastic matrix (solid phase) phase and a fluid phase filling the elastic matrix. The porous matrix gives a large friction area (contacting surface) between

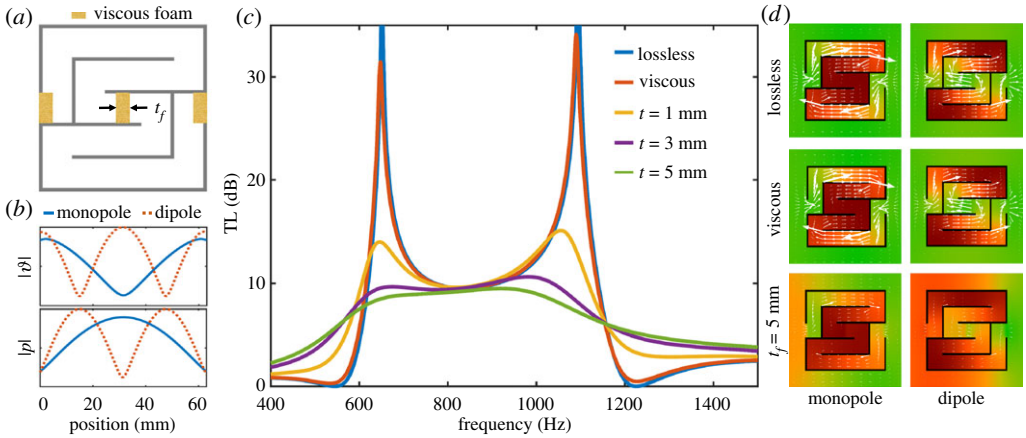

Figure 5. (*a*) Diagram of the deployment of viscous foams. All foam layers have identical thickness t_f. (*b*) Velocity and pressure profiles along the effective channel at its monopolar and dipolar modes. (*c*) TL spectra of the actual SCM with different configurations of the space-coiling channel: without thermal viscosity, with thermal viscosity and with dampening foam layers of thicknesses 1 mm, 3 mm and 5 mm. (*d*) The pressure and velocity fields at the monopole and dipole in three cases: lossless, viscous and 5 mm foam employed. The velocity representing the strength of the resonances is heavily dampened in the case of viscous foam employed, so it is called 'acoustic hyper-damping'. (Online version in colour.)

the two phases. Therefore, when submerged into a high fluid velocity region, it is expected to absorb a substantial amount of fluid flow energy. The well-known Biot model [42,43] is the most comprehensive model for describing the vibro-acoustics of the coupling between the two phases. It requires several experimental inputs, and the corresponding calculation is quite time-consuming. For this reason, the effective medium theory is used to model equivalently the porous acoustic material. Among all the existing models, the five-parameter model proposed by Johnson–Champoux–Allard (JCA) is the most widely used as it provides simplicity and high accuracy. In the JCA model, the mass density characterizing the visco-inertial effects was proposed by Johnson *et al.* [44] as

$$\widetilde{\rho}(\omega) = \frac{\tau_\infty \rho}{\varepsilon_p}\left[1 + \frac{\varepsilon_p \phi_f}{\mathrm{i}\omega\rho\tau_\infty}\sqrt{1 + \mathrm{i}\frac{4\rho\omega\eta\tau_\infty^2}{\varepsilon_p^2\phi_f^2\Lambda_v^2}}\right], \tag{3.3a}$$

and the bulk modulus is [45]

$$\widetilde{\mathcal{B}}(\omega) = \frac{\gamma P_0/\phi_f}{\gamma - (\gamma-1)\left[1 - \mathrm{i}(8k_d/\rho\omega C_p\Lambda_t^2)\sqrt{1 + \mathrm{i}(\rho\omega C_p\Lambda_t^2/16k_d)}\right]^{-1}}, \tag{3.3b}$$

where P_0 and k_d denote the fluid equilibrium pressure and thermal conductivity of the fluid phase. The five parameters of the JCA model, ε, ϕ_f, Λ_v, Λ_t and τ_∞, used to describe the acoustic foams are estimated by fitting the absorption of a pure foam layer, backed by a rigid wall under normal incidence in simulations and experiments (see electronic supplementary material). The optimal values are listed in table 1.

The TL spectra for three foam layer thicknesses, 1 mm, 3 mm and 5 mm, are presented in figure 5*c*. It is found that the local resonances of the SCM are heavily dampened. Even with the foam layers of only 1 mm thickness, the TL dips are completely removed, giving rise to the optimized TL profile. This is exactly the function of hyper-damping in the SCM. The evidence of hyper-damping can also be recognized through the velocity field inside the heavily dampened coiling channel (figure 5*d*), which represents the strength of its resonances. Since the relation between TL dips and peaks is causality [20], lifting the dips means dampening the local resonance of the SCM, which inevitably dampens the TL peaks as well. The foam thickness plays an

Table 1. Porous matrix properties of the acoustic foam.

parameter	symbol	value
porosity	ε_p	96%
flow resistivity	ϕ_f	32 000 N · s m^{-4}
viscous characteristic length	Λ_v	78 μm
thermal characteristic length	Λ_t	119 μm
tortuosity factor	τ_∞	1.83

important role in optimizing the TL profile. Increasing the foam thickness t_f leads to a relatively more uniform TL profile. When $t_f = 5$ mm, the peaks and dips are nearly unrecognizable because the SCM is over-dampened. Further increasing the foam thickness will eventually make the TL profile approach the case where the unit cell includes only ventilation channels (see electronic supplementary material). This is simply because the foam filling the effective channel results in high impedance, driving the channel to perform as a solid medium rather than as a linear acoustic channel.

4. Application in ultra-broadband sound insulation

(a) Ultra-broadband acoustic barrier

(i) Design the acoustic barrier

We employ the SCMs to construct an acoustic barrier possessing efficient ventilation (see electronic supplementary material), sound isolation and absorption functions across an ultra-broadband 0.44–0.385 kHz. This range completely covers nine third-octave bands (0.447–3.548 kHz), including the frequency spectrum of most typical airborne noise in living and working environments [1]. The target frequency range is selected such that the metamaterial barrier can work well within the stable region of the impedance tube since the cut-off frequency of the tube is around 3.85 kHz (see electronic supplementary material). The proposed barrier, as shown in figure 6*a*, consists of the super-cell bars detailed in figure 6*b*. The super-cell bar is only 220 mm thick ($t_{\text{bar}} = 220$ mm), and comprises three SCMs with the same open ratio, i.e. $\sigma_e = 1 - L/a = 29.25\%$, but different curled channel widths (5.9 mm, 7.9 mm and 11 mm). The super-cell bars without and with the dampening foam layers are considered, as shown in figure 6*b*. As presented in figure 6*c*, under normal incidence, the TL spectra of individual SCMs (see the blue, red and orange curves) show Fano profiles of not only fundamental but also higher-order resonances. They are distributed nearly uniformly over the frequency range of interest. The barrier consisting of all three SCMs under normal incident sound therefore shows satisfactory sound reduction performance (see the purple curve) within the broad region 0.3–4 kHz. However, there still exists many sharp TL dips due to the local resonances of the SCMs and the Fabry–Pérot resonances between the SCMs [31]. To get rid of these TL dips to make the high-performance band (overall >10 dB) broader and smoother, 5 mm thick foam layers are employed to introduce the acoustic hyper-damping in the acoustic barrier. The simulation result is highlighted by the green curve in figure 6*c*. Significantly better overall performance with TL dips dampened or removed is shown, although most of the TL peaks are dampened as well and even disappear. It is worth mentioning that some TL dips are even converted into peaks (at 1234 Hz corresponding to the monopolar mode of the second SCM and at 1590 Hz corresponding to the monopolar mode of the first SCM). In fact, noise usually covers a broad range of incident angle. Therefore, we also numerically investigate the angular dependence of this barrier, and show that very good sound insulation performance can be found even for a large oblique angle of incidence (see electronic supplementary material).

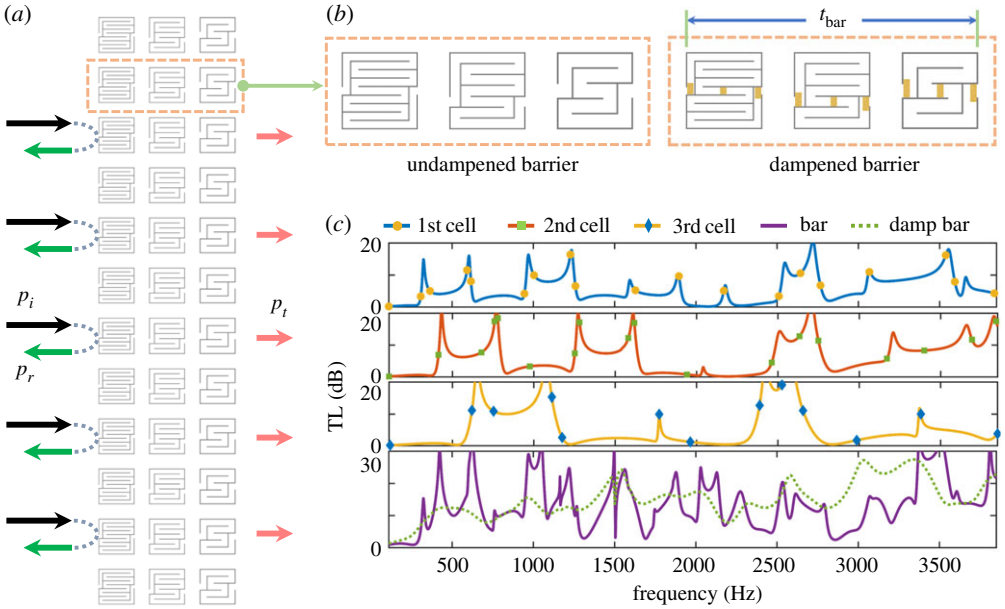

Figure 6. (*a*) Schematic of the acoustic barrier wall comprising three space-coiling cells with the same open ratio but different channel widths. (*b*) Zoom-in views of the super-cell bar without and with the dampening foam layers. (*c*) Numerically obtained transmission loss spectra of the lossless individual unit cells (blue, red and yellow curves with symbols), lossless super-cell (purple solid) and dampened super-cell (green dashed). (Online version in colour.)

(b) Experimental validation

To verify the proposed design and the simulation results, a super-cell sample is fabricated using a 3D printer. The sample containing acoustic foams, installed in the impedance tube, is shown in the inset of figure 7*a*. The performance of the super-cell, which equivalently represents the barrier's performance under normal incidence, is then evaluated in an impedance tube, as illustrated in figure 7*a*. The experimental results for the dampened acoustic barrier (see the red curves) are presented to make a comparison with the simulation results (see the blue curves) in the top panel of figure 7*b*. Good agreement is observed. The experiment exhibits ultra-broadband sound reduction performance within the range 0.3–3.85 kHz. The dampened design exhibits the TL of at least 10 dB within 0.44–3.85 kHz covering completely nine third-octave bands, with an average TL of 17.7 dB.

In addition to the TL, sound absorption of the dampened barrier defined as $A = 1 - |R|^2 - |T|^2$ is also experimentally studied. Presented in the bottom panel of figure 7*b* is the absorption of the dampened barrier under normal incidence. Overall, the simulation (blue curve) and experimental (red curve) results match well. The averaged absorption within the range 0.44–3.85 kHz is 65%. Several high-absorption bands are recognized experimentally: over 80% within the range 0.3–0.41 kHz and near 100% at 340 Hz, 490 Hz, 2965 Hz and 3810 Hz. After all, the proposed barrier, together with the acoustic hyper-damping, not only achieves ultra-broadband sound reduction while preserving ventilation efficiency but also exhibits excellent absorption capability.

5. Conclusion

We have studied, analytically, numerically and experimentally, SCMs supporting two types of Fano resonances for the realization of ultra-broadband sound reduction application. The proposed SCMs support both monopolar and dipolar modes which interact with the background continuum mode and eventually produce acoustic Fano resonances. The resultant Fano

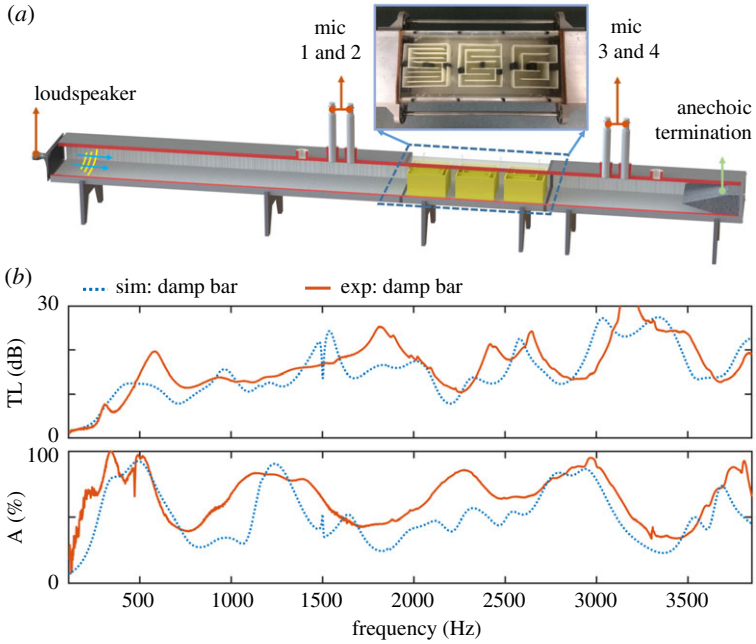

Figure 7. (*a*) Sectional view of the impedance tube and the samples in the experiment. The inset shows the detailed view of the dampened super-cell. (*b*) Comparison of the transmission loss (TL) and absorption (A) spectra between simulation and experiment results for the dampened super-cell. (Online version in colour.)

resonances are beneficial in producing ultra-broadband TL. The acoustic barrier with a thickness of 220 mm and an open ratio of 29.25%, derived from deploying periodically super-cells of three different SCM cells, shows satisfactory sound reduction performance within the broad frequency region 0.44–3.85 kHz, with the help of acoustic hyper-damping. Moreover, the acoustic absorption of the dampened barrier is measured to be overall beyond 65% with several perfect absorption regions. We believe this work paves the way for realizing effective broadband sound insulation and sound wave control devices.

Data accessibility. This article has no additional data.

Authors' contributions. H.Q.N., Q.W. and G.L.H. conceived the idea and design. H.Q.N. derived the theoretical model. H.Q.N., Q.W. and H.C. built the numerical model and performed the simulations. H.Q.N. and Q.W. fabricated samples and conducted experiments. G.L.H. and S.T. supervised the project. All authors gave final approval for publication.

Competing interests. We declare we have no competing interests.

Funding. This research was supported by Steelcase Inc.

References

1. Anon A. 2013 *E413, classification for rating sound insulation*, Philadelphia, PA: American Society for Testing and Materials.
2. García-Chocano VM, Cabrera S, Sánchez-Dehesa J. 2012 Broadband sound absorption by lattices of microperforated cylindrical shells. *Appl. Phys. Lett.* **101**, 184101. (doi:10.1063/1.4764560)
3. Thota M, Wang K. 2017 Reconfigurable origami sonic barriers with tunable bandgaps for traffic noise mitigation. *J. Appl. Phys.* **122**, 154901. (doi:10.1063/1.4991026)
4. Can A, Leclercq L, Lelong J, Botteldooren D. 2010 Traffic noise spectrum analysis: dynamic modeling vs. experimental observations. *Appl. Acoust.* **71**, 764–770. (doi:10.1016/j.apacoust.2010.04.002)
5. Ingard U. 2009 *Noise reduction analysis*. Boston, MA: Jones & Bartlett Publishers.

6. Nguyen H, Huang G. 2019 Multiple Helmholtz resonator based acoustic liner. In *Health monitoring of structural and biological systems XIII*, vol. 10972 (eds P Fromme, Z Su). Denver, CO: International Society for Optics and Photonics SPIE.
7. Kurrasch AJ. 1991 *Acoustic panel*. US Patent no. 5,009,043.
8. Kinsler LE, Frey AR, Coppens AB, Sanders JV. 1999 *Fundamentals of acoustics*. New York, NY: John Wiley & Son, Inc.
9. Chen Y, Zhu R, Nguyen H, Huang G. 2015 Membrane-type acoustic metamaterials: theory, design, and application. In *Theory and design of acoustic metamaterials* (eds PF Pai, G Huang), pp. 52–102. Washington, DC: SPIE Press.
10. Hirsekorn M. 2004 Small-size sonic crystals with strong attenuation bands in the audible frequency range. *Appl. Phys. Lett.* **84**, 3364–3366. (doi:10.1063/1.1723688)
11. Sánchez-Dehesa J, Garcia-Chocano VM, Torrent D, Cervera F, Cabrera S, Simon F. 2011 Noise control by sonic crystal barriers made of recycled materials. *J. Acoust. Soc. Am.* **129**, 1173–1183. (doi:10.1121/1.3531815)
12. Garcı VM *et al.* 2013 Optimum control of broadband noise by arrays of cylindrical units made of a recycled material. *Appl. Acoust.* **74**, 58–62. (doi:10.1016/j.apacoust.2012.06.008)
13. Nguyen H, Wu Q, Xu X, Chen H, Tracy S, Huang G. 2020 Broadband acoustic silencer with ventilation based on slit-type Helmholtz resonators. *Appl. Phys. Lett.* **117**, 134103. (doi:10.1063/5.0024018)
14. Koussa F, Defrance J, Jean P, Blanc-Benon P. 2012 Transport noise reduction by low height sonic crystal noise barriers. In *Proc. of Acoustics, Nantes, France, 23–27 April 2012*, pp. 1004–1007. See http://www.conforg.fr/acoustics2012/cdrom/data/articles/000004.pdf.
15. Cheng Y, Zhou C, Yuan B, Wu D, Wei Q, Liu X. 2015 Ultra-sparse metasurface for high reflection of low-frequency sound based on artificial Mie resonances. *Nat. Mater.* **14**, 1013–1019. (doi:10.1038/nmat4393)
16. Liang Z, Li J. 2012 Extreme acoustic metamaterial by coiling up space. *Phys. Rev. Lett.* **108**, 114301. (doi:10.1103/PhysRevLett.108.114301)
17. Ghaffarivardavagh R, Nikolajczyk J, Holt RG, Anderson S, Zhang X. 2018 Horn-like space-coiling metamaterials toward simultaneous phase and amplitude modulation. *Nat. Commun.* **9**, 1–8. (doi:10.1038/s41467-018-03839-z)
18. Fano U. 1961 Effects of configuration interaction on intensities and phase shifts. *Phys. Rev.* **124**, 1866. (doi:10.1103/PhysRev.124.1866)
19. Joe YS, Satanin AM, Kim CS. 2006 Classical analogy of Fano resonances. *Phys. Scr.* **74**, 259. (doi:10.1088/0031-8949/74/2/020)
20. Miroshnichenko AE, Flach S, Kivshar YS. 2010 Fano resonances in nanoscale structures. *Rev. Mod. Phys.* **82**, 2257. (doi:10.1103/RevModPhys.82.2257)
21. Rau A. 2004 Perspectives on the Fano resonance formula. *Phys. Scr.* **69**, C10. (doi:10.1238/Physica.Regular.069a00C10)
22. Lee T, Nomura T, Su X, Iizuka H. 2020 Fano-like acoustic resonance for subwavelength directional sensing: 0–360 degree measurement. *Adv. Sci.* **7**, 1903101. (doi:10.1002/advs.201903101)
23. Ghaffarivardavagh R, Nikolajczyk J, Anderson S, Zhang X. 2019 Ultra-open acoustic metamaterial silencer based on Fano-like interference. *Phys. Rev. B* **99**, 024302. (doi:10.1103/PhysRevB.99.024302)
24. Ingard U. 1953 On the theory and design of acoustic resonators. *J. Acoust. Soc. Am.* **25**, 1037–1061. (doi:10.1121/1.1907235)
25. Yang Z, Mei J, Yang M, Chan N, Sheng P. 2008 Membrane-type acoustic metamaterial with negative dynamic mass. *Phys. Rev. Lett.* **101**, 204301. (doi:10.1103/PhysRevLett.101.204301)
26. Fang N, Xi D, Xu J, Ambati M, Srituravanich W, Sun C, Zhang X. 2006 Ultrasonic metamaterials with negative modulus. *Nat. Mater.* **5**, 452–456. (doi:10.1038/nmat1644)
27. Zhang X, Liu Z. 2004 Negative refraction of acoustic waves in two-dimensional phononic crystals. *Appl. Phys. Lett.* **85**, 341–343. (doi:10.1063/1.1772854)
28. Xie Y, Wang W, Chen H, Konneker A, Popa BI, Cummer SA. 2014 Wavefront modulation and subwavelength diffractive acoustics with an acoustic metasurface. *Nat. Commun.* **5**, 1–5.
29. Nguyen H. 2018 Acoustic metasurface harvester. In *INTER-NOISE and NOISE-CON Congress and Conf. Proc.*, pp. 5787–5795. Chicago, IL: Institute of Noise Control Engineering.
30. Ma G, Yang M, Xiao S, Yang Z, Sheng P. 2014 Acoustic metasurface with hybrid resonances. *Nat. Mater.* **13**, 873–878. (doi:10.1038/nmat3994)

31. Nguyen H, Huang G. 2020 Perfect absorption in duct by coupling Helmholtz resonators. In *INTER-NOISE and NOISE-CON Congress and Conf. Proc.*, vol. 262, pp. 859–865. New Orleans, LA: Institute of Noise Control Engineering.
32. Li J, Wang W, Xie Y, Popa BI, Cummer SA. 2016 A sound absorbing metasurface with coupled resonators. *Appl. Phys. Lett.* **109**, 091908. (doi:10.1063/1.4961671)
33. Zhou Y, Fang X, Li D, Hao T, Li Y. 2018 Acoustic multiband double negativity from coupled single-negative resonators. *Phys. Rev. Appl.* **10**, 044006. (doi:10.1103/PhysRevApplied.10.044006)
34. Sun M, Fang X, Mao D, Wang X, Li Y. 2020 Broadband acoustic ventilation barriers. *Phys. Rev. Appl.* **13**, 044028. (doi:10.1103/PhysRevApplied.13.044028)
35. Xiong L, Bi W, Aurégan Y. 2016 Fano resonance scatterings in waveguides with impedance boundary conditions. *J. Acoust. Soc. Am.* **139**, 764–772. (doi:10.1121/1.4941568)
36. Yang M, Chen S, Fu C, Sheng P. 2017 Optimal sound-absorbing structures. *Mater. Horiz.* **4**, 673–680. (doi:10.1039/C7MH00129K)
37. Liu C, Long H, Zhou C, Cheng Y, Liu X. 2020 Reversed Doppler effect based on hybridized acoustic Mie resonances. *Sci. Rep.* **10**, 1–7. (doi:10.1038/s41598-019-56847-4)
38. Nguyen H, Zhu R, Chen J, Tracy S, Huang G. 2018 Analytical coupled modeling of a magneto-based acoustic metamaterial harvester. *Smart Mater. Struct.* **27**, 055010. (doi:10.1088/1361-665X/aab993)
39. Ingard U. 1954 Transmission of sound through a stretched membrane. *J. Acoust. Soc. Am.* **26**, 99–101. (doi:10.1121/1.1907298)
40. Allard J, Atalla N. 2009 *Propagation of sound in porous media: modelling sound absorbing materials*, 2nd edn. New York, NY: John Wiley & Sons.
41. Stinson MR. 1991 The propagation of plane sound waves in narrow and wide circular tubes, and generalization to uniform tubes of arbitrary cross-sectional shape. *J. Acoust. Soc. Am.* **89**, 550–558. (doi:10.1121/1.400379)
42. Biot MA. 1956 Theory of propagation of elastic waves in a fluid-saturated porous solid. II. Higher frequency range. *J. Acoust. Soc. Am.* **28**, 179–191. (doi:10.1121/1.1908241)
43. Biot MA. 1956 Theory of propagation of elastic waves in a fluid-saturated porous solid. II. Higher frequency range. *J. Acoust. Soc. Am.* **28**, 179–191. (doi:10.1121/1.1908241)
44. Johnson DL, Koplik J, Dashen R. 1987 Theory of dynamic permeability and tortuosity in fluid-saturated porous media. *J. Fluid Mech.* **176**, 379–402. (doi:10.1017/S0022112087000727)
45. Champoux Y, Allard JF. 1991 Dynamic tortuosity and bulk modulus in air-saturated porous media. *J. Appl. Phys.* **70**, 1975–1979. (doi:10.1063/1.349482)